

# Experimental testing of data fusion in a distributed ground-based sensing network for Advanced Air Mobility

Federica Vitiello<sup>1</sup> Flavia Causa<sup>2</sup> Roberto Opromolla<sup>3</sup> Giancarmine Fasano<sup>4</sup>

*University of Naples “Federico II”, Piazzale Tecchio 80, Naples, 80125, Italy*

Chester Dolph<sup>5</sup> Todd Ferrante<sup>6</sup>

*NASA Langley Research Center, 1 Nasa Dr, Hampton, VA, 23666, USA*

Thomas Lombaerts<sup>7</sup> Corey Ippolito<sup>7</sup>

*NASA Ames Research Center, Moffett Field, CA, 94035, USA*

**Advanced Air Mobility (AAM) is an active area of development which foresees the integration of autonomous uncrewed aircraft into the civil airspace for air transportation of people and cargo. Safe integration requires significant technological developments and extensive testing phases of sensing and surveillance strategies in dense airspace. Compared to well-assessed manned aviation systems scenarios, surveillance strategies in the AAM and small Uncrewed Aircraft Vehicles (UAVs) context need to detect smaller platforms flying at lower altitude against cluttered backgrounds in dense airspace. Fusion of data provided by a network of distributed sensing nodes is a powerful tool to enable detection and tracking in such complex conditions. This paper contributes to this research direction by proposing a surveillance strategy for the AAM environment based on sensor fusion of data acquired by distributed ground-based radars. Specifically, experimental data collected with two independent radars, observing the flight of two small UAVs, are used. Data fusion at tracking level is based on a leader-helper strategy where the leader radar uses the helper’s measurements to increase the lifespan of its generated tracks. This solution shows promising results with a 10% increase in track coverage with respect to the standalone leader radar tracking solution. The paper also proposes an interference removal processing method which is applied on the data collected by one of the two radars.**

## I. Introduction

Advanced Air Mobility (AAM) is a concept of operation for air transportation which has emerged together with the fast technological development in the field of the Uncrewed Aircraft Vehicles (UAVs) and electric Vertical Take-

---

<sup>1</sup> PhD Candidate, Department of Industrial Engineering, University of Naples “Federico II”.

<sup>2</sup> Postdoctoral Research fellow, Department of Industrial Engineering, University of Naples “Federico II”.

<sup>3</sup> Assistant Professor, Department of Industrial Engineering, University of Naples “Federico II”.

<sup>4</sup> Associate Professor, Department of Industrial Engineering, University of Naples “Federico II”.

<sup>5</sup> Aeronautics Systems Engineering, NASA Langley Research Center. AIAA Member.

<sup>6</sup> Analytical Mechanics Associates, Inc. NASA Langley Research Center.

<sup>7</sup> KBR Wyle Services, NASA Ames Research Center.

<sup>8</sup> Aerospace Scientist, Intelligent Systems Division. NASA Ames. AIAA Senior Member.

Off and Landing (eVTOL) aircraft. AAM envisions the use of UAV and eVTOL for the mobility of people and goods between places which are hardly or less efficiently reached by the traditional aviation means. This novel transportation paradigm, thus, will require enabling highly autonomous operations especially in low-altitude conditions. Safety is paramount for UAV and AAM, and it's even more relevant during flights over urban areas. In these regards, the term Urban Air Mobility (UAM) can be more properly used, to identify a subset of AAM which foresees the transportation task in and around metropolitan areas. AAM and UAM are bound to radically transform the air transportation market by promoting a shift from scheduled operations to on-demand ones [1]. In this environment, platforms such as air taxis [2], commuting people around urban areas, will operate alongside platforms performing package deliveries, either for private parties or for medical first responders [3], within a highly dense air traffic scenario.

Recent research and development aims to ensure safe integration of these novel platforms within the civil airspace. Relevant studies are focused on the investigation of both social/economical aspects potentially affecting the air transportation market [4] as well as on regulatory [5] and technological aspects. In this latter perspective, technological innovations in several systems, including both onboard avionics and air traffic control/management and surveillance systems, are needed to achieve the technological maturity level required to support the forecasted highly dynamic and highly dense volumes of operations. From this latter point of view, a key enabler for the UAM/AAM vision is the design of a surveillance solution tailored for the detection of small platforms flying relatively close to the ground. In this field, the efficacy of cooperative traffic monitoring systems relying on the broadcast of information from the surrounding traffic, via Automatic Dependent Surveillance-Broadcast (ADS-B) transponders for instance, can be weakened by the absence or unreliability of Global Navigation Satellite Systems (GNSS) information typical of urban areas. Although studies are addressing this issue by adding secondary positioning information sources [6], the overall surveillance solution needs to also be robust towards malicious intrusions within a given flight volume, either air corridors or near vertiports (i.e., take-off and landing areas for UAVs and eVTOL). In this scenario, non-cooperative sensing strategies need to be developed. The exploitation of technologies such as visual cameras and radars for such strategies has been widely studied [7], [8]. However, the performance of both sensors can degrade in the presence of small targets (such as small UAVs) characterized by low detectability, especially when they fly in proximity to ground. For instance, reference [9] highlights a reduction in the detection range provided by visual-based solutions, while reference [10] discusses the challenges of detecting small UAVs in the presence of clutter in radar data, instead. Sensor fusion strategies can be a powerful tool to overcome the limitations of purely visual- or radar-based techniques. By leveraging on their complementary characteristics, highly accurate angular measurements (typical of visual cameras) as well as range and range rate measurements (typical of Doppler radars) can be achieved. Such advantage in the sensing solution accuracy was discussed in [11], where a radar/visual fusion strategy exploiting different visual detection approaches was tested on experimental data involving a small UAV. Specifically, a hierarchical fusion solution was used where the radar acted as the main sensor for the generation of firm tracks, i.e., highest reliability tracks, while the camera served as an aiding sensor by acting only after firm track generation. A radar/visual fusion tracker was also presented and compared with standalone sensor strategies in [12]: tests on data from the simulated flights of two UAVs showed the noisier nature of radar data with respect to visual data, causing the estimated track to diverge from the true one during camera dropouts.

The fusion of data from radars and cameras located in the same area does not allow a complete coverage of the airspace to be surveyed, especially if large in extension. In this case, a robust solution would consist in a set of independent distributed sensors capturing the flight space, thus taking advantage of the spatial diversity of single sensor measurements within the fused solution. The exploitation of a network of sensors to collect information on small UAV is an active area of research in the initial stages of investigation. The NASA Revolutionary Aviation Mobility (RAM) subproject of the Transformational Tools and Technology (TTT) project is researching the development of distributed sensing architecture for UAM and SUAS in the AAM context [13]. A distributed sensing approach was also discussed in [14], where a simulation environment was used to replicate the flight of an eVTOL over the San Francisco Bay, observed by a set of seven cameras and two radars. These simulations show that the cameras play a significant role in improving both the noisy measurements of radar data and the accuracy of the tracking estimates. However, such accuracy deteriorates with the decrease in the number of cameras observing the targets.

This paper follows the research thread on distributed networks of sensors using data collected from a joint experiment between TTT AAM projects. During the experiments a distributed sensing network with three independent ground nodes, each equipped with a radar and camera, collected data of HDV flight operations [15] at the NASA Langley City Environment Range Testing for Autonomous Integrated Navigation (CERTAIN) flight space [16]. Specifically, an innovative distributed fusion strategy exploiting two radars capturing the flight of two small UAVs operated by HDV, is here proposed. In the designed fusion solution, tracking algorithms whose structure is described in [11] run on the data of each radar in an independent fashion. Once a firm track is generated, the generating radar is elected as "leader" and starts exploiting the measurements retrieved by the other radar ("helper") when needed. The

exchange of data from the helper to the leader is only enabled when the leader's tracks are at risk of being deleted (due to lack of associated measurements). Therefore, the role of the helper is to attempt extending the time length of the leader's firm tracks thus aiming to reduce track dropouts. It is worth highlighting that although the developed strategy is tested on two radars only, it can easily be scaled to accommodate the introduction of additional helper radars. The strategy assumes that a data link between the radars can be established to support the sharing of measurements. In the considered experiments, it has been tested offline on the collected data.

In general, track dropouts can be caused by geometrical constraints, i.e., object occlusions produced by fixed obstacles in the Field Of View (FOV) of the sensor, as well as by sensor-related phenomena, such as interference when multiple radars operate in the same area. The process of removing interference-affected radar data is challenging as it can lead to discard valid measurements of flying targets. Thus, as an additional contribution, this paper proposes a radar interference mitigation method. While many studies address the characterization of radar data to remove ground-based clutter, which is especially relevant to the detection of small UAVs with low Radar Cross Sections (RCS) [17], this is the first work which also deals with radar interference removal for the detection of small UAV using field collected data.

This paper is organized as follows. In section II, the methodology used for radar interference removal and for the leader-helper radars fusion strategy is presented. Section III introduces the experimental activities carried out along with the sensors setup and UAV trajectories. Section IV shows the results achieved with the designed radar sensing solution. Finally, section V provides a conclusion to this work.

## II. Distributed Radar Fusion Methodology

### A. Radar Interference And Clutter Removal

Radar data used for the proposed distributed sensing strategy is affected by the presence of clutter which arises from fixed objects (such as the ground or near-by buildings, for instance) in terms of direct or indirect, i.e., multipath, reflections, as well as from internal, device-driven phenomena. To reduce the amount of undesired measurements, which are not of interest for the tracking process, data pre-processing steps were designed and implemented in recent research [10]. These steps include a filtering procedure, which reduces clutter by applying thresholds on the measured range rate ( $\dot{r}$ ) and RCS. Specifically, measurements which verify  $\dot{r} < \dot{r}_{th,low}$  are declared as clutter-based detections and are thus discarded. Furthermore, measurements which verify  $RCS < RCS_{th,low}$  and  $RCS > RCS_{th,up}$  are also discarded to reduce the amount of information not corresponding to the UAV. By exploiting a priori knowledge of the environment where the radars operate (and accounting for their known locations), the corresponding measurement space can be restricted by setting filters on the range ( $r$ ), azimuth ( $az$ ) and elevation ( $el$ ) angles.

Unfortunately, the application of these filters is not enough to prevent the collection of outliers due to interference phenomena deriving from the partial overlap between the FOVs of radars in the distributed sensing network. If unmitigated, radar interference can degrade the quality of the data passed over to the tracker by generating excessive number of false tracks and lose information relevant to the targets of interest (i.e., the small UAVs). The interference phenomenon, which affects one of the two radars exploited in this work, is observed in terms of a large number of detections retrieved in the same radar beam (same values of  $az$  and  $el$  which define the center of the beam) and showing wide variations in  $r$ , RCS and  $\dot{r}$ . The retrieval of multiple detections in the same beam, thus at the same pointing direction, is a common occurrence for electronically-scanning array radars and results from the physical dimensions of the beam, which determines the angular accuracy of the radar. Still, when interference takes place, this phenomenon is enormously enhanced due to the reception of signals emitted by other radars. Such signals are received by the radar which translates them into range measurements due to their shift in frequency. The proposed filtering procedure leverages on the variability of the range measurements retrieved in the same beam. Specifically, the method detects interference when, at a given  $az-el$  pointing direction, a set of more than two detections show a standard deviation in their range measurements which is larger than a threshold  $r_{sth}$ . The value selected for  $r_{sth}$  (along with all the other setting parameters) is detailed in the results section.

### B. Leader-Helper Distributed Radar Fusion Strategy

A flow diagram of the proposed radar fusion strategy is shown in Fig. 1. Each radar tracker exploits a Nearly Constant Velocity EKF model to estimate the state of all detected objects. In the following discussion, the subscript  $k$  is used to refer to the different radars, either acting as leader,  $l$ , or as helper,  $h$ . The EKF state vector is defined as follows,  $\mathbf{x}_k = [x_k, y_k, z_k, \dot{x}_k, \dot{y}_k, \dot{z}_k]^{NED}$ , thus containing the components of the relative position ( $x_k, y_k, z_k$ ) and velocity ( $\dot{x}_k, \dot{y}_k, \dot{z}_k$ ) vectors of the tracked object with respect to the radar in the local North-East-Down (NED) reference frame centered at the radar location. The measurement vector used in the EKF correction step is defined as  $\mathbf{z}_k = [r_k, az_k, el_k, \dot{r}_k]^{NED}$ . Such vector contains the range ( $r_k$ ), azimuth ( $az_k$ ), elevation ( $el_k$ ) and range rate ( $\dot{r}_k$ ) in the NED frame as pre-processed to

mitigate interference and clutter effects (as previously discussed in subsection II.A). Each set of measurements is first retrieved within the Radar-centered Reference Frame (RRF) and then rotated in NED by exploiting the knowledge of the attitude of the sensor, parametrized as a 3-2-1 sequence of Euler angles, heading ( $\psi$ ), pitch ( $\theta$ ) and roll ( $\phi$ ) or, equivalently, as a rotation matrix ( $M_{\text{NED}}^{\text{RRF}}$ ).

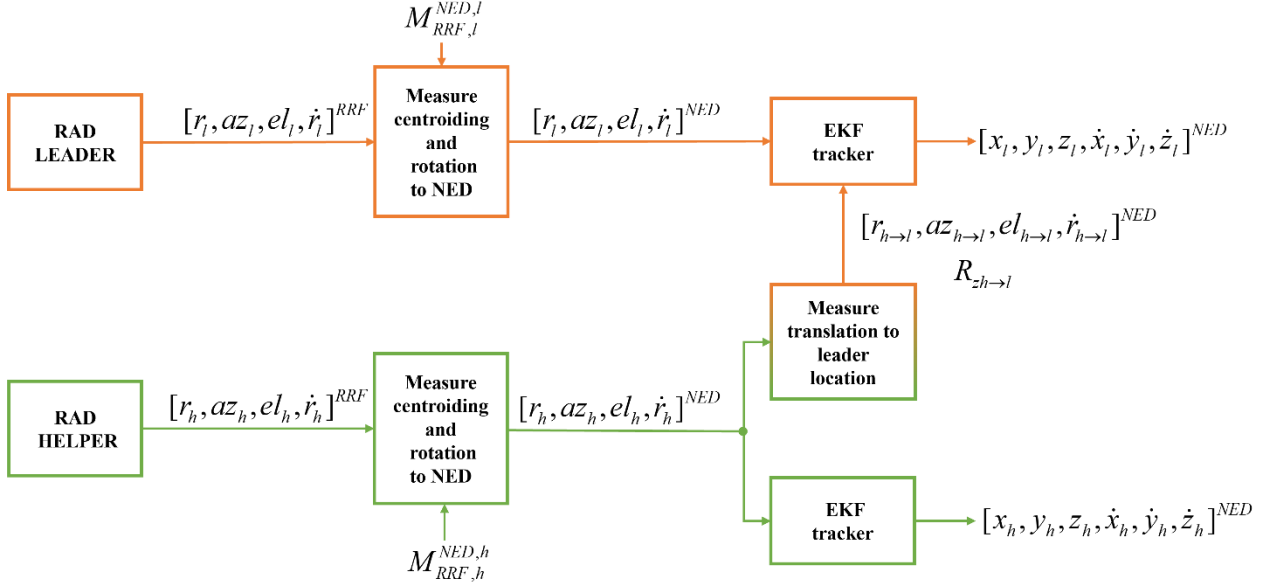


**Fig. 1** Flow diagram of the developed leader-helper radar fusion sensing strategy. The term RAD indicates a radar-based sensing node.

Before such rotation is performed, measurements undergo a centroiding procedure which is used to cluster the detections retrieved at the same time-stamp and likely belonging to the same target. To decide if a set of measurements with the same time stamp can be clustered, their range, azimuth, and elevation values are compared. Specifically, if the difference in range, azimuth and elevation of two or more measurements is smaller than a corresponding threshold indicated as  $\delta r$ ,  $\delta az$  and  $\delta el$ , respectively, a cluster is identified. Hence, a unique average measurement in range, azimuth, elevation and range rate is computed for each cluster.

The EKF trackers follow the logic previously described in [10]. Hence, initial track attempts, i.e., one-plot tracks, are generated from first (or unassociated) radar detections, and their reliability is increased over time passing through tentative tracks and leading to firm (or confirmed) tracks, by exploiting measurement-to-track association criteria based on the Mahalanobis distance ( $\xi_k$ ) computed as shown in Eq. (1). Here,  $P_k$  is the state covariance matrix,  $R_{z_k}$  is the measurement covariance matrix,  $H_k$  is the jacobian matrix of the measurement with respect to the state and, finally,  $\hat{z}_k$  is the predicted measurement.

$$\xi_k = (\mathbf{z}_k - \hat{\mathbf{z}}_k)^T (H_k P_k H_k^T + R_{z_k})^{-1} (\mathbf{z}_k - \hat{\mathbf{z}}_k) \quad (1)$$

When measurements lack or their association is not successful, tracks are propagated in time by exploiting the EKF prediction step. If such prediction is performed for a time ( $dt_{pred}$ ) larger than a threshold ( $dt_{FT}$  for firm tracks), a track is deleted.

During the tracking procedure, when the first firm track is generated by either of the two trackers the generating radar is elected as leader while the other is considered as a helper, instead. Then, both radars continue their tracking (based on [11]) independently. However, the leader tracker will start using the helper's measurements whenever one of its generated firm tracks is at risk of being deleted. Therefore, in the leader case, a further measurement-to-track association step is attempted to extend its soon-to-end firm tracks based on the helper's measurements. Specifically, such measurements are injected in the leader's tracker when one of its firm tracks verifies the condition  $dt_{FT}/2 \leq dt_{pred} \leq dt_{FT}$ . Measurements collected by the helper radar are referred to the NED reference which is centered at its location ( $\mathbf{X}_h=[X_h, Y_h, Z_h]$ ), rather than the leader one ( $\mathbf{X}_l=[X_l, Y_l, Z_l]$ ). Therefore, a translational transform must be applied to the helper's measurements within the leader EKF. To this aim, first, the relationship  $\mathbf{x}_h=g(\mathbf{z}_h)$ , transforming

the spherical measurement (contained in the vector  $\mathbf{z}_h$ ) in a cartesian measurement (contained in the vector  $\mathbf{x}_h$ ) through the non-linear function  $g$ , shown in Eq. (2), is applied.

$$\begin{bmatrix} x_h \\ y_h \\ z_h \\ \dot{x}_h \\ \dot{y}_h \\ \dot{z}_h \end{bmatrix} = \begin{bmatrix} r_h \cos(az_h) \cos(el_h) \\ r_h \sin(az_h) \cos(el_h) \\ -r_h \sin(el_h) \\ r_h \cos(az_h) \cos(el_h) \\ r_h \sin(az_h) \cos(el_h) \\ -r_h \sin(el_h) \end{bmatrix} \quad (2)$$

Then, the measurement vector in cartesian coordinates is translated to the leader's location ( $\mathbf{x}_{h \rightarrow l}$ ) using the relationship  $\mathbf{x}_{h \rightarrow l} = \mathbf{x}_h + \Delta \mathbf{X}$  where  $\Delta \mathbf{X} = [X_h - X_l, Y_h - Y_l, Z_h - Z_l, 0, 0, 0]$  is the vector containing the relative position and velocity of the helper location with respect to the leader one. The relative velocity components listed in  $\Delta \mathbf{X}$  are all equal to zero m/s due to the fixed location of the two devices. Once translated, the measurement vector can be converted back to spherical coordinates by exploiting the relationship  $\mathbf{z}_{h \rightarrow l} = h(\mathbf{x}_{h \rightarrow l})$ , as shown in Eq. (3).

$$\begin{bmatrix} r_{h \rightarrow l} \\ az_{h \rightarrow l} \\ el_{h \rightarrow l} \\ r_{h \rightarrow l} \end{bmatrix} = \begin{bmatrix} \sqrt{x_{h \rightarrow l}^2 + y_{h \rightarrow l}^2 + z_{h \rightarrow l}^2} \\ tg^{-1} \left( \frac{y_{h \rightarrow l}}{x_{h \rightarrow l}} \right) \\ -\sin^{-1} \left( \frac{z_{h \rightarrow l}}{\sqrt{x_{h \rightarrow l}^2 + y_{h \rightarrow l}^2 + z_{h \rightarrow l}^2}} \right) \\ \frac{x_{h \rightarrow l} \dot{x}_{h \rightarrow l} + y_{h \rightarrow l} \dot{y}_{h \rightarrow l} + z_{h \rightarrow l} \dot{z}_{h \rightarrow l}}{\sqrt{x_{h \rightarrow l}^2 + y_{h \rightarrow l}^2 + z_{h \rightarrow l}^2}} \end{bmatrix} \quad (3)$$

This coordinate system transformation introduces an additional uncertainty in the helper radar measurement. Such uncertainty is related to the errors in the GNSS-based-localization of both devices whose information is contained in the matrix  $\Sigma_{GNSS}$  of Eq. (4) where the covariances ( $\sigma$ ), arising from the GNSS measurements along each direction, are listed. This effect also needs to be accounted for when measurements are passed over to the leader radar. To do so the measurement covariance matrix ( $\mathbf{R}_{z_{h \rightarrow l}}$ ), associated with the  $\mathbf{z}_{h \rightarrow l}$  vector, is computed. Firstly, the helper radar measurement covariance matrix ( $\mathbf{R}_{z_h}$ ) is transformed in its cartesian expression ( $\mathbf{R}_{x_h}$ ) exploiting the relationship  $\mathbf{R}_{x_h} = \mathbf{D} \mathbf{R}_{z_h} \mathbf{D}^T$ , where the matrix  $\mathbf{D}$  is the jacobian of the spherical-to-cartesian transformation, obtained from derivation of equation (2). Then, the matrix  $\mathbf{R}_{x_{h \rightarrow l}}$ , representing the uncertainty in cartesian coordinates of the helper measurement translated to the leader location, can be computed as  $\mathbf{R}_{x_{h \rightarrow l}} = \mathbf{R}_{x_h} + \Sigma_{GNSS}$ , and it can then be transformed into a spherically-expressed matrix exploiting the relationship  $\mathbf{R}_{z_{h \rightarrow l}} = \mathbf{H} \mathbf{R}_{x_{h \rightarrow l}} \mathbf{H}^T$ . Here,  $\mathbf{H}$  is the jacobian of the spherical-to-cartesian transformation, obtained from derivation of equation (3).

$$\Sigma_{GNSS} = \begin{bmatrix} \Sigma_{POS} & \mathbf{0}_{3 \times 3} \\ \mathbf{0}_{3 \times 3} & \Sigma_{VEL} \end{bmatrix}, \Sigma_{POS} = \begin{bmatrix} \sigma_{x,h}^2 + \sigma_{x,l}^2 & 0 & 0 \\ 0 & \sigma_{y,h}^2 + \sigma_{y,l}^2 & 0 \\ 0 & 0 & \sigma_{z,h}^2 + \sigma_{z,l}^2 \end{bmatrix}, \Sigma_{VEL} = \mathbf{0}_{3 \times 3} = \begin{bmatrix} 0 & 0 & 0 \\ 0 & 0 & 0 \\ 0 & 0 & 0 \end{bmatrix} \quad (4)$$

### III. Experimental Activities

Data used for this work was collected during experimental campaigns where a set of up to three different sensing nodes, located around the CERTAIN Range flight-testing field, was used to observe the flight of small UAVs. The UAVs were flown within the HDV NASA sub-project, which demonstrated the feasibility of a realistic AAM/UAM air traffic scenario by operating up to five UAVs simultaneously. An overview of the experimental activities carried out can be found in [19]. NASA designed, developed, and built the sensor configurations described below.

Each of the sensing node was equipped with an Echoflight radar (Frequency Modulated Continuous Wave radar manufactured by Echodyne), visual cameras and a GNSS receiver and antenna. The UAVs were Alta-8 platforms (manufactured by Freefly), which are small octocopters with maximum unfolded dimension of about 1.3 meters. The mission performed by such platforms during the HDV flights involved the autonomous travel over a waypoint-based trajectory starting and ending in their vertiport location. Fig. 2 shows a snapshot from one of the flight days, with

multiple Alta-8 on their respective vertipads. The data used for the development of this specific work, was acquired during the flight of two Alta-8 platforms, with tail numbers “N556NU” and “N561NU”. These platforms autonomously performed a 7-minutes loop around the CERTAIN range, reaching a maximum transverse distance from their vertipad of about 500 meters and a maximum altitude slightly over 100 meters. A 3D visualization of the trajectory flown by the UAV in the NED reference frame is shown in Fig. 3. During take-off, the UAV reached 40 meters in altitude, which was then increased up to 100 meters during the first climbing phase of the loop. A second climbing phase followed, bringing the vehicles to a maximum altitude of 110 meters which was then kept constant before starting the descent phase. During the latter, the UAVs descended back to 40 meters in altitude before landing at their vertipad location. The two vehicles performed such pattern keeping a fixed distance one from the other. This was made possible by properly arranging the scheduling of departures, i.e., by having N556NU as the first platform to depart and N561NU following after about 1 minute.

Radar and camera data observing such flight were recorded using three ground sensing nodes. Such nodes were located at the head of the field (“wythe creek” node), on the gantry structure (“gantry” node), and on top of a building’s roof (“rooftop” node). The location of the nodes is shown both in the 3D visualization of Fig. 3 and on the satellite map in Fig. 4. In the former, the different heights at which nodes were located can be easily noticed. The gantry node, in fact, was mounted at a height of about 60 meters with respect to the ground, while the rooftop node was directed approximately 10 meters above ground. In Fig. 4, the FOV of the radars is depicted, thus giving an idea of the direction towards which the nodes were pointed. It is important to clarify that the sensors were rigidly mounted on their node structure, therefore, the pointing direction of the single sensor can be referred to the whole node. To retrieve an accurate estimate of the attitude of the radars in the NED reference, the QUaternion ESTimation (QUEST) algorithm [18] can be exploited. In this case the position of the UAVs, retrieved by their onboard GNSS receivers, is used. The results of the application of such algorithm in terms of the 3-2-1 sequence of Euler angles are reported in Table I for the three radars.

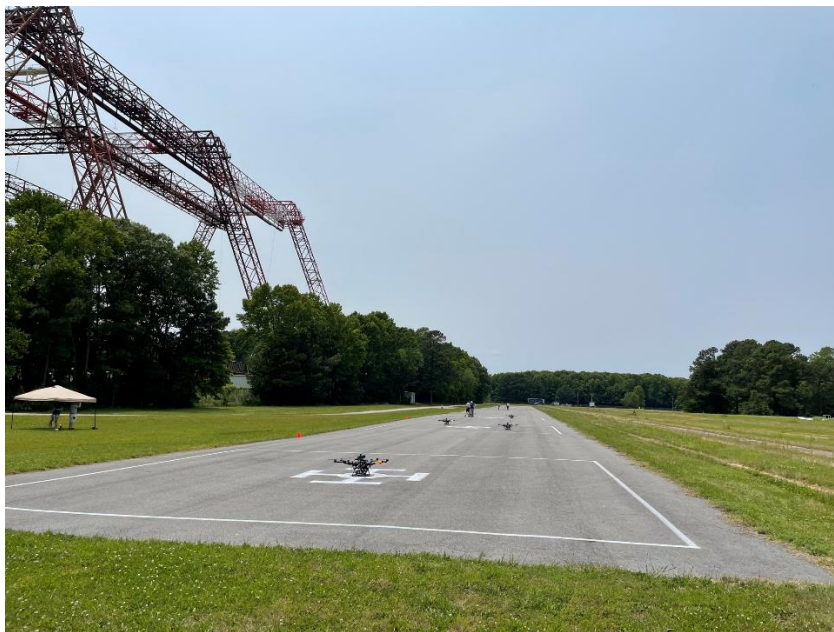


**Fig. 2** Alta-8 UAVs on the vertipads during flight preparation in one of the flight campaigns performed by the HDV subproject. Photo taken at the NASA Langley CERTAIN Range.

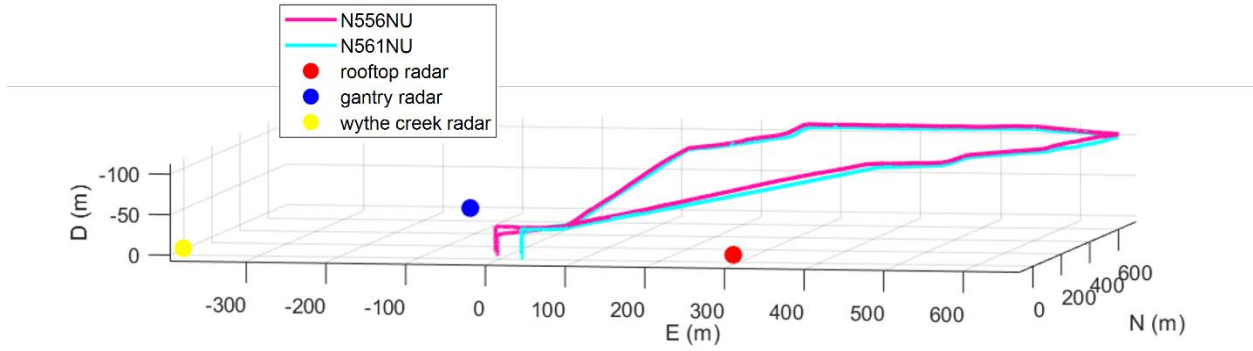


**Fig. 3** 3D visualization of the trajectory flown by the two UAVs in the NED reference frame. Position of radars shown as colored dots. The direction of the third (Down) axis is reversed to ease the understanding of the trajectory altitude.



**Fig. 4** Satellite map over the CERTAIN Range flight area at NASA Langley. Trajectories flown by the UAVs are reported along with the position of the ground nodes operated during the flight. The FOVs of the radars are shown as faded triangles starting from the respective location (colored dots).

**Table I** Results of the attitude estimation for all radar using QUEST.

Radar Location	$\psi$	$\theta$	$\phi$
Rooftop	$-5^\circ$	$7.5^\circ$	$1^\circ$
Gantry	$32.9^\circ$	$2.7^\circ$	$0.4^\circ$
Wythe creek	$87.6^\circ$	$3.4^\circ$	$4^\circ$

In the top row of Fig. 5, the gantry and rooftop nodes are shown in their respective locations during one of the flight days, while their constitutive components are shown in greater details in the bottom row. The data acquired by the radars mounted on such nodes are used for the purpose of this work, thus, the description of the wythe creek node components is here omitted. The Echoflight radars operate by generating a sequence of beams to scan a FOV with fixed size along the horizontal (azimuth) and vertical (elevation) directions, generating a scanning pattern which can be repeated differently depending on the exploited operative mode, either search or search-while-track. In the latter, the scanning process is frequently interrupted by the device, which prioritizes the revisit of areas of the FOV where

detections were found. All radars utilized the search-while-track mode and retrieved measurements at a frequency of about 10 Hz. While the radars can scan a FOV of  $120^\circ$  in the horizontal direction and  $80^\circ$  in the vertical direction, the extensions used during the acquisition were reduced for the specific location of the node as appropriate. Specifically, in the rooftop case, the minimum elevation value was reduced to avoid the introduction of measurements arising from ground clutter. Minimum and maximum values of azimuth and elevation, defining the size of the scanned FOV, are reported in Table II.

The acquisition of each node's sensor was achieved by remotely accessing the onboard processing units via cellular link. Different types of software were used to acquire the data from the nodes. In the rooftop case, the Robot Operating System (ROS) environment was used to build a launch file which could simultaneously control and acquire data from its radar, camera and GNSS receiver. In the gantry case, two different acquisition software scripts were written in C++ programming language to launch radar with GNSS and the camera respectively. For the sake of completeness, it must be highlighted that the gantry node is the only one to be equipped with multiple cameras and processing units. Each processing unit is dedicated to the acquisition of one camera, but a single processing unit (i.e., the central one, highlighted in light blue in Fig. 5 bottom-left) is used to acquire data from the GNSS receiver, radar and central camera. The Ublox F9P GNSS receiver was used on each node with a patch antenna.

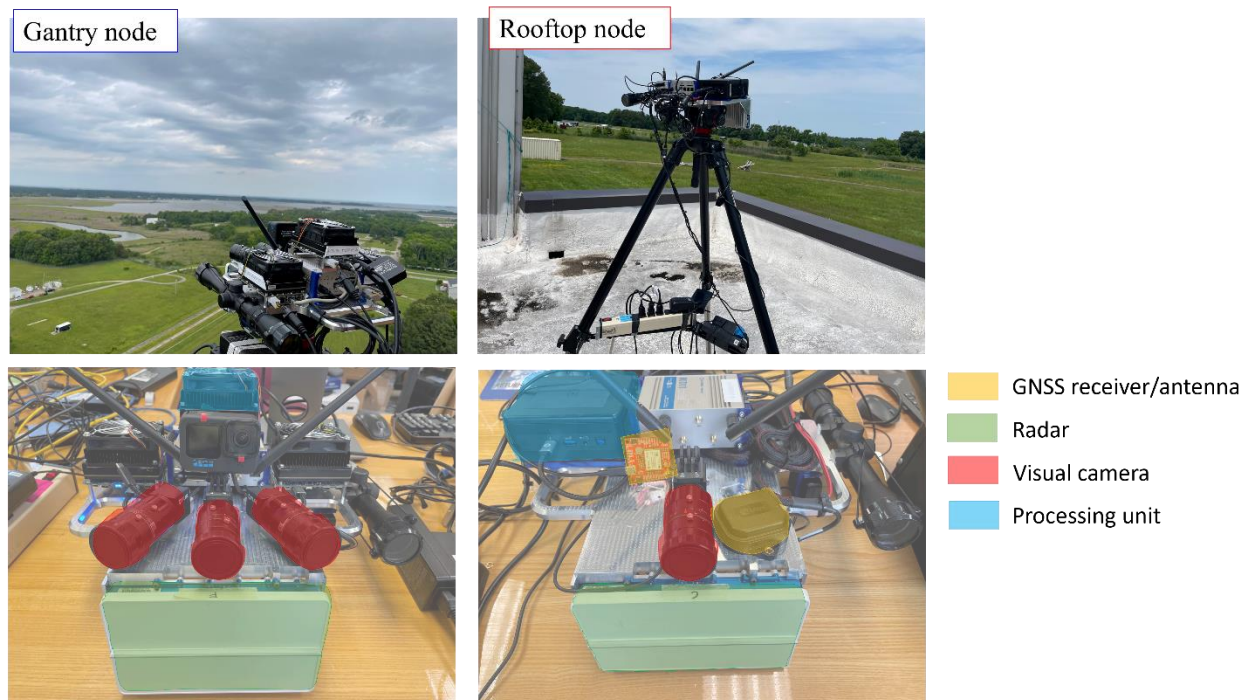


**Fig. 5** Top row: gantry (left) and rooftop (right) nodes during one acquisition. Bottom row: Devices on gantry (left) and rooftop (right) nodes. The GNSS receiver is not shown on gantry node.

**Table II** Extensions of the FOV of the gantry and rooftop radars.

Radar Location	$az_{min} - az_{max}$	$el_{min} - el_{max}$
Rooftop	$-60^\circ - 60^\circ$	$-6^\circ - 40^\circ$
Gantry	$-60^\circ - 60^\circ$	$-40^\circ - 40^\circ$

## IV. Experimental Results

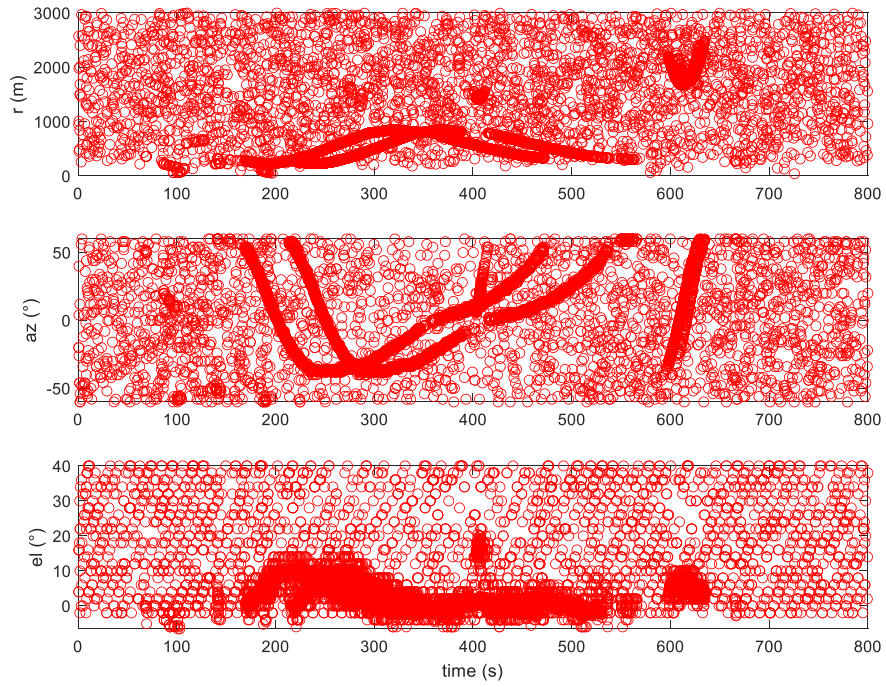
### A. Radar Interference and Clutter Removal

Fig. 7 and Fig. 6 show the raw measurements acquired by the two radars in their own RRF coordinates. Although the two radars retrieve measurements up to a distance of 6000 meters the plots are constrained from 0 meters to 3000

meters to ease the understanding of the presented data. A difference between the behavior and distribution of measurements from the two radars can immediately be noticed. In the rooftop case (Fig. 6), measurements belonging to the two UAVs can be seen in the time interval going from 200 seconds to almost 600 seconds. Additional targets are also detected by the radar, summing up to about 12400 single detections over 13 minutes of acquisition. The distribution of most of detections is spread widely over  $r$ ,  $az$  and  $el$ , which traces their generation back to the clutter effect. In the gantry case (Fig. 7), it is difficult to see any measurement corresponding to the flying UAVs. Here, the occurrence of interference-generated measurements can be observed in terms of bands of range measurements which appear to be concentrated around given time instants and which show a high variation, extending over the whole range span. This large amount of data yielded a total number of about 59600 single detections, which is almost five times greater than the rooftop radar's acquisitions. To understand such a difference in the data, the radars' geometrical disposition needs to be considered. While the rooftop radar was placed at a more distant location with respect to the wythe creek and gantry ones, it was also physically shielded by the presence of obstacles along the line of sight with the other devices (such as the building structure and the tree line). The gantry radar was completely exposed to the presence of the wythe creek radar and their FOVs overlapped at a shorter distance.

The filtering strategies applied to the two radars are based on the a priori knowledge of the environment where they operated and their geometrical disposition. In the rooftop case, filtering is only applied based on the measurements of  $\dot{r}$ ,  $r$  and RCS by exploiting the thresholds  $\dot{r}_{th,low}=0.9$  m/s,  $RCS_{th,low}=-25$  dBsm and  $RCS_{th,up}=0$  dBsm. An additional filter is then also applied to only retain data corresponding to range measurements below 1200 meters. The application of these filters reduces the clutter and noise as shown in the filtered data for the rooftop radar of Fig. 8, thus reducing the number of single measurements down to 3638. Applying the filtering technique is not as effective in removing the interference-caused range bands for the gantry. Thus, the interference detection and removal strategy discussed in section II is applied using a value of  $r_{oth}=50$  meters. This makes it possible to completely remove the presence of the range bands. However, due to the very large vertical FOV set for the gantry radar, additional filters are applied on the elevation value, thus removing all detections arising from the ground (i.e., with elevation smaller than  $-30^\circ$ ). A further analysis to identify the presence of other objects (such as transmitting antennas), potentially generating noise in radar measurements, is also performed on such data.

After interference removal and data filtering process the radar measurements appear to be much clearer and more suitable to be used during tracking with a total number of measurements substantially reduced to 2586. This reduction is paid in terms of the reduction in useful measurements belonging to the UAVs as well. These can be identified by exploiting the positioning information logged by the UAVs autopilots and computing the difference between the radar range measurements and the GNSS-based range (with respect to the radar location). Measurements can then be inferred to UAVs if such difference is smaller than a threshold which is set to 3 meters. This method yields a loss of about 44% and 40% of measurements for the first and second UAV, respectively. The measurements retrieved after filtering on the gantry radar are shown in Fig. 9.



**Fig. 6** Unprocessed radar measurements collected by the rooftop radar. Only data belonging to a measured range of up to 3000 meters are reported.

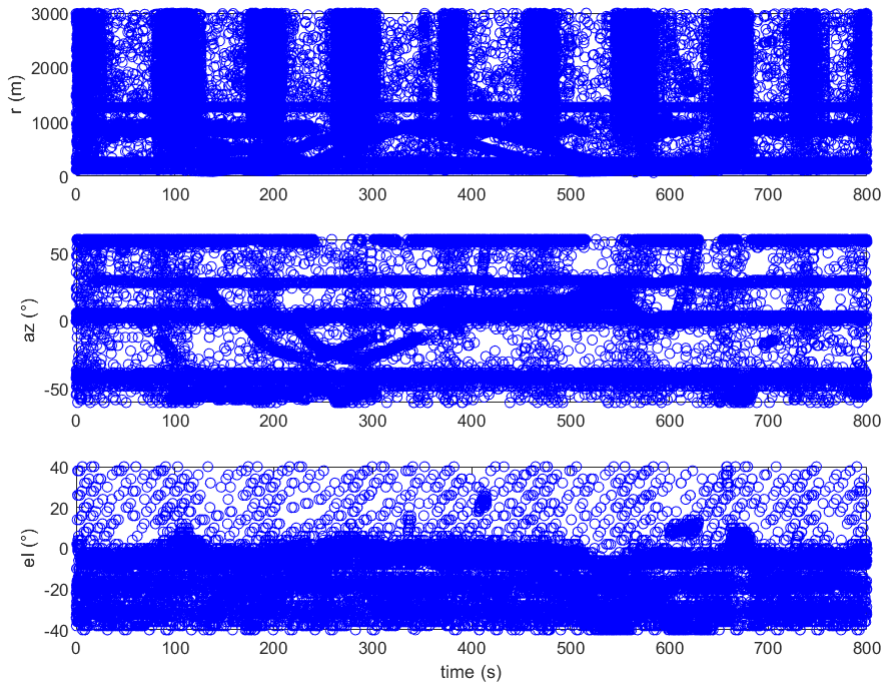


**Fig. 7** Unprocessed radar measurements collected by the gantry radar. Only data belonging to a measured range of up to 3000 meters are reported.

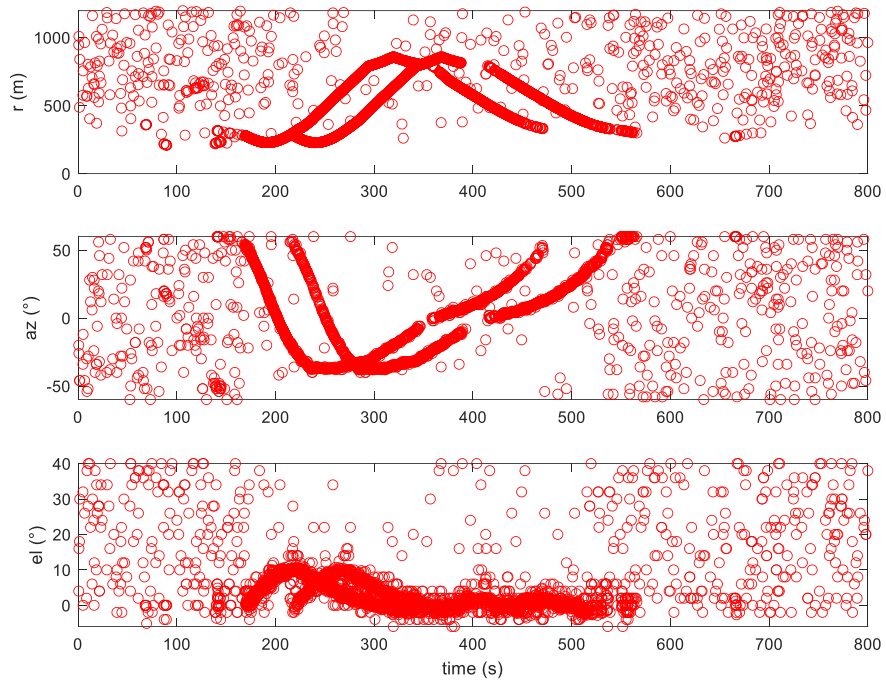


**Fig. 8** Filtered radar measurements collected by the rooftop radar.

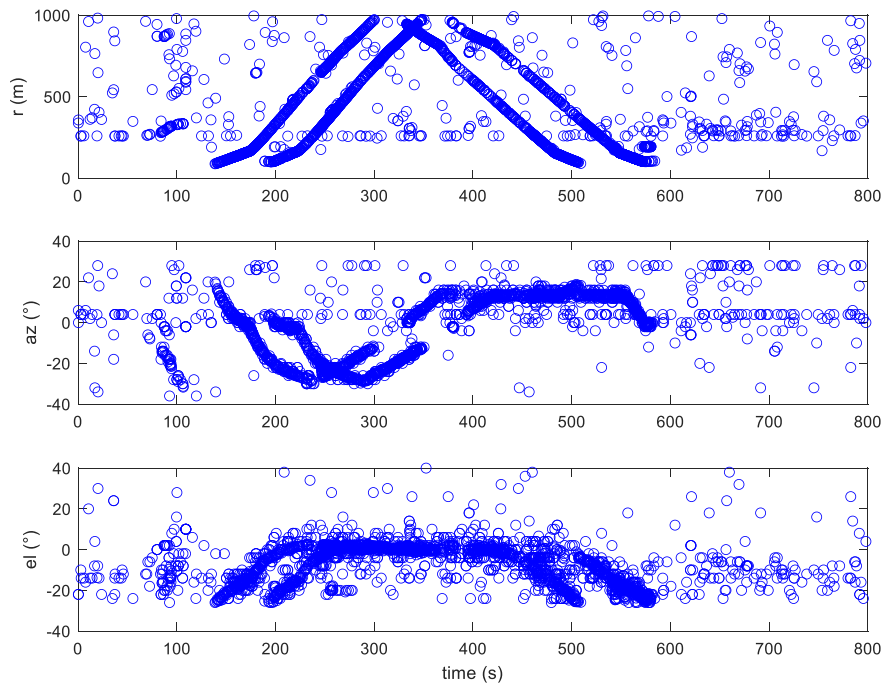


**Fig. 9** Filtered radar measurements collected by the gantry radar.

## B. Leader-Helper Distributed Radar Fusion Strategy

Results achieved on the fused radar tracking strategy presented in section II are discussed here. The proposed EKF makes use of a time step of 0.1 seconds, thus being comparable to the acquisition frequency of radar measurements. As a consequence of the complex data filtering process many valid radar measurements are lost. This is even more evident in the case of the gantry radar, where the interference removal process causes loss of useful information belonging to the UAVs. The fusion of data collected by a network of sensors distributed along the flight field can help reduce track dropouts caused by such losses. In the case of firm tracks, dropouts occur when the prediction steps are performed for more than  $dt_{FT}=4$  seconds. To better highlight advantages in using the distributed fusion strategy, the standalone radar tracking solution of the leader radar is compared to the fused one, in which the helper radar injects its measurements. In both standalone and fused solutions, measurements are first centroided before being passed over to the tracker. During the centroiding, the values of  $\delta r=6$  meters,  $\delta az=2^\circ$  and  $\delta el=12^\circ$  are used.

During the tracking process, the two radars are used independently until the leader is established. This happens when the first radar retrieves a firm track. The second radar, thus, acts as helper and it continues its tracking independently while also sharing useful data with the leader upon need. In the tested case, the first radar to retrieve a firm track is the gantry radar. Therefore, its standalone EKF-retrieved solution is used as a mean of comparison for the fusion strategy performance. The GNSS positioning information collected and processed by the autopilot of each UAV is taken as ground truth to extract accuracy of the firm tracking estimates. Finally, the difference in track coverage between the fused and standalone results is presented. Specifically, track coverage represents the ratio between the actual presence of the UAV within the FOV of the radar and the presence of an estimate of the UAV state from the tracker.

In the following figures, the results of the firm tracking solutions are shown in terms of the estimated  $r$ ,  $az$  and  $el$  in the NED reference frame along with the reference ground truth. The first values are reported with the subscript “FT”, while the latter are reported with the subscript “GT”. Fig. 10 shows both the results achieved on the standalone gantry radar (left) and the results achieved when such radar acts as the leader being aided by the rooftop radar (right). The leader radar appears to be able to generate tracks of the two UAVs during their flight starting at about 20 seconds from their appearance within the radar FOV (when the UAV elevation is larger than  $-30^\circ$ ). The multi-object nature of the exploited tracker makes it possible to generate and keep separate tracks of multiple objects at the same time. Tracks that cannot be associated to the UAV are reported as “other” in the figure. Some of such tracks show steep azimuth and elevation variations and may be generated by birds flying around the flight area while others, whose temporal length is comparable to  $dt_{FT}$ , arise from noise or unremoved clutter measurements. The longest-living tracks generated by the standalone leader tracker correspond to the UAVs, thus demonstrating the adequacy of the data pre-processing step, which is tailored for the preservation of measurements related to the UAV. Still, frequent tracks interruptions (dropouts), caused by measurement losses, occur in these tracks. These dropouts, though not affecting the maximum range at which UAVs are tracked (around 990 meters for both vehicles), cause an intermittent behavior in the UAV tracks, thus promoting the generation of three and five different tracks for N556NU and N561NU, respectively. The use of additional information retrieved by the helper radar and shared with the leader can be a powerful tool during dropouts. This can immediately be noticed by looking at the right part of Fig. 10, where the results of the fused leader-helper strategy are depicted. In this case, a continuous, unique track of the first UAV (N556NU) is generated with no dropout while, in the case of N561NU, two different tracks are generated, instead. This result promotes the increase of the track coverage which goes from 88.38% to 97.18%, for N556NU, and from 87.42% to 95.84%, for N561NU.

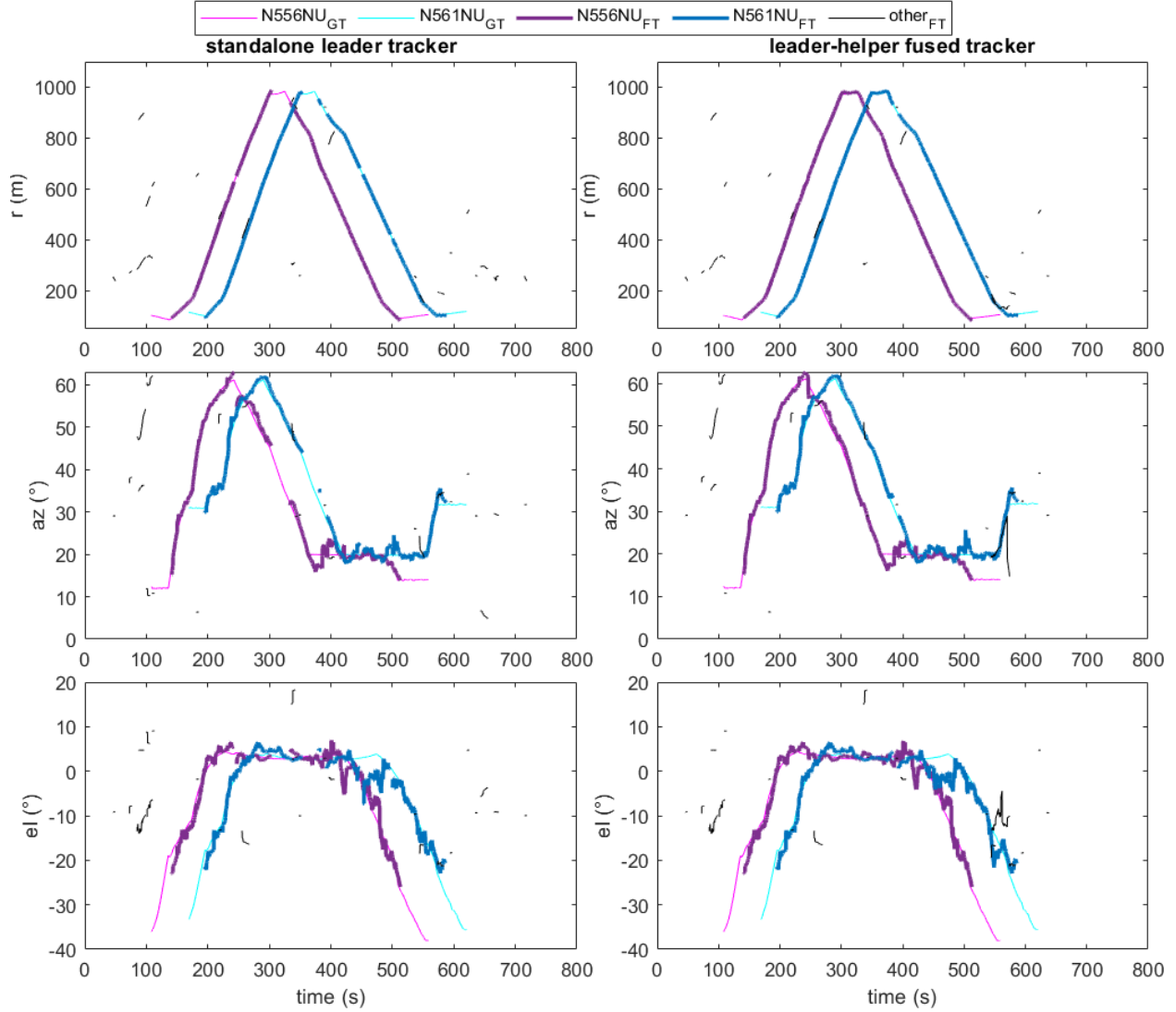


**Fig. 10** Results of the tracking procedure with the standalone leader radar (left) and the fused leader-helper strategy (right). Results are shown in terms of range, azimuth and elevation in NED with respect to time.

A comparison is also done in terms of tracking accuracy by computing the difference between the estimate from firm tracking and the ground-truth for each UAV. This is shown in terms of range ( $\Delta r$ ), azimuth ( $\Delta az$ ) and elevation ( $\Delta el$ ) in Fig. 11 for the firm tracks of the two UAVs only. In this context, no real benefit in the use of the fused solution is identified. Indeed, if the root mean square (rms) errors of each difference are computed (as reported in Table III), a slight increase can be noticed when the fused solution is used. However, this is only verified in the range case while the angular rms values appear to be comparable for both cases. This occurrence can be related to the higher value of the range uncertainty contained within the  $R_{zh \rightarrow l}$  matrix, which is used by the leader to filter its track with the helper's measurement. The range uncertainty increases, due to the translation of measurements between two different locations, at high ranges. The leader tracker completely loses information about the UAV at a range of 900 meters and is able to successfully associate helper's measurements to extend its tracks' life. However, the uncertainty related to such measurement is higher with respect to the uncertainty of the leader's measurements, thus causing localized increases in the distance between the estimates and the ground truth.

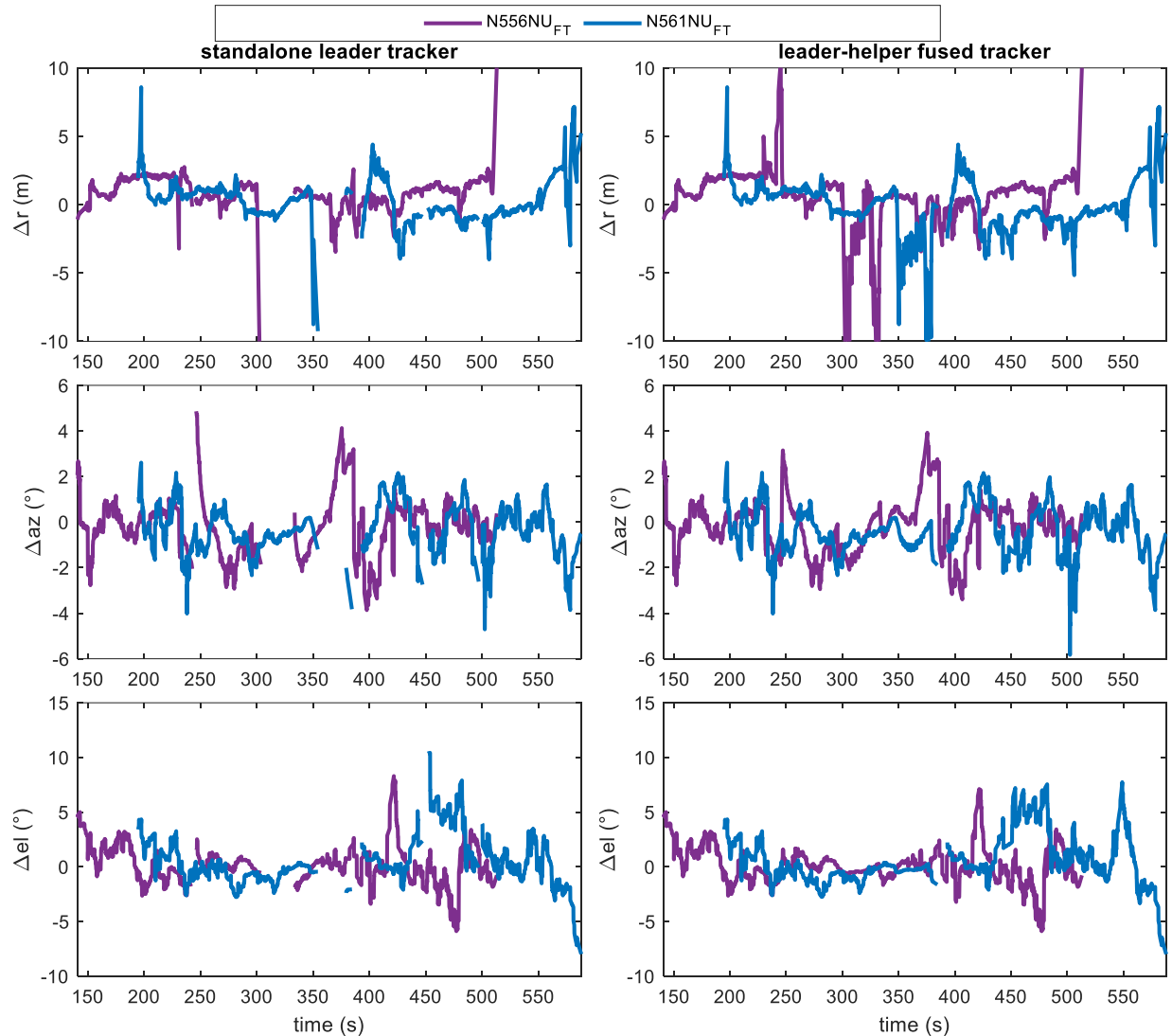


**Fig. 11** Difference between the tracking estimate and the ground-truth (based on GNSS positioning from the UAV autopilot) for the standalone (left) and fused (right) strategies.

**Table III** Root mean square error of the firm tracking estimates with respect to the ground truth.

UAV	$\Delta r$		$\Delta az$		$\Delta el$	
	Standalone	Fused	Standalone	Fused	Standalone	Fused
N556NU	1.74 m	2.31 m	1.31°	1.18°	1.86°	1.70°
N561NU	1.71 m	2.03 m	1.18°	1.14°	2.43°	2.40°

## V. Conclusion

This paper presents an innovative radar fusion strategy tailored for a distributed network of radars for future AAM/UAM scenarios. Specifically, the strategy is tested offline on data collected during experimental tests which involved three operating FMCW radars. Radars were mounted on ground-based nodes placed in specific locations and at different heights, observing the flight of two UAVs. To prove the efficacy of the strategy, two radars among the three are used in this work. The proposed fusion solution involves the use of a leader radar, which is the first to retrieve a firm track, and a helper radar, which shares its measurements with the leader. The solution assumes that a data link between the radars can be established and, therefore, to reduce data transmission needs in then communication network, measurements from the helper are only used by the leader when its firm tracks are at risk of being deleted

due to the lack of associated measurements for a relatively long-time span. The strategy proved its efficacy in increasing tracking coverage almost up to 10% with respect to the standalone radar solution, while causing only a slight decrease in accuracy due to the necessary coordinate transformation process.

The paper also focuses on the pre-processing data steps needed to remove clutter and noise from radar data, as well as false detections caused by interference phenomena occurring in the presence of an overlap between the FOVs of the radars in the sensing network. The adopted interference removal strategy leverages on the unphysical effect of retrieving measurements which vary strongly in range with no real variation in azimuth and elevation. The results of this methodology show that interference can be effectively removed at the cost of losing a percentage of valid measurements.

The developed data processing and fusion strategy shows promising results. However, future works will be focused on its further improvements which can be achieved tackling different aspects. First, the hierarchical strategy with which a leader radar is elected will be compared to different strategies in which all measurements from all active radars are used when available. This latter approach will be studied aiming to promote an improvement in the accuracy of the tracking estimate which will benefit from the spatial diversity of the retrieved measurements. A final sensing solution exploiting all the information retrieved by the ground-based nodes will be designed by incorporating visual data as well. Finally, future developments will also focus on the characterization of the radar interference phenomenon, thus paving the way to the design of a robust sensing strategy for a network of distributed active sensors.

### Acknowledgments

Research performed by the University of Naples “Federico II” was carried out in the frame of project “CREATEFORUAS”, funded within Programme PRIN by the Italian Ministry of Education, University and Research. NASA’s contribution was completed in support of TTT project milestones. The authors would like to thank Lou Glaab and Jacob Shaeffer for facilitating the HDV+TTT joint activity, Matt Coldsnow for his help with safety reviews, Zackary Mitchell for his assistance in data acquisition, Greg Howland for initial CAD work (AMA), SUAS pilots Mark Motter, Jody Miller, and Brayden Chamberlain, Range Safety Officers Mark Frye and Jennifer Fowler, and interns Yajvan Ravan and Aref Malek.

### References

- [1] B. J. Holmes, and R. A. Parker, “A Vision and Opportunity for Transformation of On-Demand Air Mobility,” *16th AIAA Aviation Technology, Integration, and Operations Conference*, AIAA AVIATION Forum, AIAA 2016-3465, Jun. 2016. doi: 10.2514/6.2016-3465.
- [2] Uber Air | Uber Elevate. <https://www.uber.com/it/it/elevate/>. Accessed on November 25<sup>th</sup> 2023.
- [3] The Project | SAFIR-Med. <https://www.safir-med.eu/project>. Accessed on November 25<sup>th</sup> 2023.
- [4] B. A. Hamilton, "Urban Air Mobility (UAM) Market Study: Final Report." National Aeronautics and Space Administration (NASA). Available online: <https://ntrs.nasa.gov/citations/20190001472> (accessed on 2 June 2020), 2018.
- [5] C. Xu, X. Liao, J. Tan, H. Ye, and H. Lu, “Recent Research Progress of Unmanned Aerial Vehicle Regulation Policies and Technologies in Urban Low Altitude,” *IEEE Access*, vol. 8, pp. 74175–74194, 2020, doi: 10.1109/ACCESS.2020.2987622.
- [6] Lum, C. W., Larson, R., Handley, W., Lui, S., & Caratao, Z., “Flight Testing an ADS-B Equipped sUAS in GPS-Denied Environments”. In *AIAA Flight Testing Conference*, p. 3139, 2017.
- [7] J. Lai, J. J. Ford, L. Mejias, and P. O’Shea, “Characterization of sky-region morphological-temporal airborne collision detection,” *J Field Robot*, vol. 30, no. 2, pp. 171–193, Mar. 2013, doi: 10.1002/rob.21443.
- [8] T. Kotegawa, “Proof-of-concept airborne sense and avoid system with ACAS-XU flight test,” *IEEE Aerospace and Electronic Systems Magazine*, vol. 31, no. 9, pp. 53–62, Sep. 2016, doi: 10.1109/MAES.2016.150163.
- [9] R. Opromolla and G. Fasano, “Visual-based obstacle detection and tracking, and conflict detection for small UAS sense and avoid,” *Aerosp Sci Technol*, vol. 119, Dec. 2021, doi: 10.1016/j.ast.2021.107167.
- [10] P. Poitevin, M. Pelletier and P. Lamontagne, "Challenges in detecting UAS with radar," 2017 International Carnahan Conference on Security Technology (ICCST), Madrid, Spain, 2017, pp. 1-6, doi: 10.1109/CCST.2017.8167852.
- [11] F. Vitiello, F. Causa, R. Opromolla, and G. Fasano, “Ground-to-air experimental assessment of low SWaP radar-optical fusion strategies for low altitude Sense and Avoid,” *2022 IEEE/AIAA 41st Digital Avionics Systems Conference (DASC)*, Portsmouth, VA, USA, 2022, pp. 1-10. doi: 10.1109/DASC55683.2022.9925826.
- [12] T. Lombaerts, K. H. Shish, G. Keller, V. Stepanyan, N. Cramer, and C. Ippolito, “Adaptive Multi-Sensor Fusion Based Object Tracking for Autonomous Urban Air Mobility Operations,” in *AIAA Science and Technology Forum and Exposition, AIAA SciTech Forum 2022*, San Diego, CA, USA, 2022. doi: 10.2514/6.2022-0362.
- [13] C. Ippolito, K. Hashemi, E. Kawamura, G. E. Gorospe, W. Holforthy, K. Kannan, V. Stepanyan, T. Lombaerts, N. Brown, A. J. Jaffe, C. Dolph, “Concepts for Distributed Sensing and Collaborative Airspace Autonomy in Advanced Urban Air Mobility”, in *AIAA Science and Technology Forum and Exposition, AIAA SciTech Forum 2023*, National Harbor, MD, USA, 2023

- [14] T. Lombaerts, T., K. Kannan, E. Kawamura, C. Dolph, V. Stepanyan, G. E. Gorospe, & C. Ippolito., "Distributed Ground Sensor Fusion Based Object Tracking for Autonomous Advanced Air Mobility Operations." in *AIAA Science and Technology Forum and Exposition*, AIAA SciTech Forum 2023, National Harbor, MD, USA, 2023. <https://doi.org/10.2514/6.2023-0896>.
- [15] L. J. Glaab, M. A. Johnson, R. G. McSwain, S. C. Geuther, Q. V. Dao and J. R. Homola, "The High Density Vertiplex Advanced Onboard Automation Overview," *2022 IEEE/AIAA 41st Digital Avionics Systems Conference (DASC)*, Portsmouth, VA, USA, 2022, pp. 1-10, doi: 10.1109/DASC55683.2022.9925834.
- [16] J. Brown, "CERTAIN City Environment Range Testing for Autonomous Integrated Navigation". Available online: <https://ntrs.nasa.gov/citations/20160009254>, 2016.
- [17] W. Hwang, H. Jang, M. Choi, "Clutter Cancellation Methods for Small Target Detection Using High-Resolution W-band Radar". *Sensors*. 2023; 23(17):7557. <https://doi.org/10.3390/s23177557>.
- [18] M. D. Shuster and S. D. Oh, "Three-axis Attitude Determination From Vector Observations", *Journal of Guidance Control and Dynamics*, vol. 4, no. 1, pp. 70-77, 19, 1981.
- [19] C. Dolph, T. Lombaerts, V. Stepanyan, E. Kawamura, K. Kannan, G. Szatkowski, T. Ferrante, C. Morris, F. Vitiello, F. Causa, R. Opromolla, and G. Fasano, "Distributed Sensor Fusion of Ground and Air Nodes using Vision and Radar Modalities for Tracking Multirotor Small Uncrewed Air Systems and Birds" in *AIAA Science and Technology Forum and Exposition*, AIAA SciTech Forum 2024, Orlando, FL, USA, 2024.